

Abstract

Quantification of heat and constituent transport by gravity waves in global models is challenging due to limited model resolutions. Current parameterization schemes suffer from over-simplification and often underestimate the transport rate. In this study, a new approach is explored to quantify the effective vertical eddy diffusion by using a high-resolution WACCM simulation based on scale invariance. The WACCM simulation can partially resolve the mesoscale gravity wave spectrum down to 250 km horizontal wavelength, and the heat flux and the effective vertical eddy diffusion by these waves are calculated directly. The effective vertical diffusion by the smaller-scale, unresolved waves, is then deduced based on scale invariance, following the method outlined by Liu (2019) in quantifying gravity wave momentum flux and forcing. The effective vertical diffusion obtained is generally larger than that obtained from parameterizations, and is comparable with that derived from observations in the mesosphere and lower thermosphere region.

Plain Language Summary

Atmospheric gravity waves may transport heat and chemical species in the vertical direction. Such transport, often measured in terms of an effective diffusion over the large-scale background atmosphere, can be important in controlling the exchange of energy and mass between the lower and upper atmosphere, but quantification of the transport process is challenging because gravity waves are not well resolved or not resolved at all in global models. Previous formulation to approximate the transport tends to oversimplify the process, and can lead to model biases. In high resolution models, the larger scale part of the gravity waves are resolved and the transport by these waves can be directly calculated from simulation results. This study shows that the transport flux of heat follows scale invariance—a statistical similarity over scales—within the resolved mesoscale range. This scale invariance is used to derive the transport flux by the unresolved waves. It is shown that the transport by the unresolved waves can contribute significantly to the total wave transport. The effective diffusion coefficient derived from this study is comparable to values obtained from observations.

1 Introduction

Gravity waves (GWs) play a critical role in transporting momentum, heat and constituents throughout the atmosphere. Their effects need to be parameterized in general circulation models (GCMs), because GWs are a sub-grid scale process (Alexander et al., 2010). This was demonstrated as being essential to model the zonal wind reversal and the anomalous winter-to-summer temperature gradient in the mesosphere/mesopause region by Holton (1982, 1983), who used the linear saturation theory (Lindzen, 1981) to parameterize the drag by breaking GWs. It is also shown in later studies that GW drag is important for driving the stratospheric quasi-biennial oscillation (QBO) (Baldwin et al., 2001) and the mesospheric semi-annual oscillation (MSAO) (Dunkerton, 1982; Sassi & Garcia, 1997).

GW dissipation is found to induce a net heat flux, which has been determined from a linear theory (Walterscheid, 1981). This is in addition to the diffusion by turbulence induced by GW breaking as formulated in Lindzen (1981). The same idea applies to the transport of constituents, and the wave induced heat/constituent flux has been formulated in terms of an effective eddy diffusion coefficient (Garcia et al., 2007; A. Z. Liu, 2009; Gardner & Liu, 2010). The formulation by Garcia et al. (2007) is applied in the Whole Atmosphere Community Climate Model (WACCM). Although diffusion from gravity wave breaking is found to play a secondary role in tracer transport in comparison to advection (Holton & Schoeberl, 1988), WACCM simulations by Garcia et al. (2014) demonstrated that the CO₂ distribution above ~80 km depends sensitively on the effective eddy diffusion coefficient. Furthermore, the values from WACCM (~5 to 50 m²s⁻¹ between

60 80–100 km) are found to be smaller than those determined from observations (Swenson
 61 et al., 2019), and those required for achieving agreement with various measurements of
 62 constituents (Feng et al., 2013; Garcia et al., 2014; Randall et al., 2015; Orsolini et al.,
 63 2017; Smith-Johnsen et al., 2018).

64 Beyond monochromatic wave consideration, Walterscheid and Hocking (1991) sug-
 65 gested that the superposition of a random set of GWs may result in significant parcel
 66 dispersion and vertical diffusion in the mesosphere and lower thermosphere (MLT), based
 67 on a quasi-linear theory and parcel trajectory simulations. The same study also suggests
 68 that the eddy diffusion coefficient obtained from wave flux calculation can oscillate be-
 69 tween large down-gradient (positive) and counter-gradient (negative) values.

70 The combined effects of superposition of transient, finite amplitude, and dissipat-
 71 ing GWs associated with a myriad of wave sources are not tractable analytically and thus
 72 not easily parameterized. Modeling study by GCMs, on the other hand, also faces its
 73 own challenges. The foremost challenge is the forbidding cost of simulating the full range
 74 of mesoscale GWs, including the wave sources, wave propagation, and wave dissipation
 75 in the whole atmosphere environment. It is, however, possible for whole atmosphere mod-
 76 els to partially resolve the GW spectrum with the current computing power down to sev-
 77 eral hundred km (e.g., H.-L. Liu et al. (2014); Becker and Vadas (2018)). Effective eddy
 78 diffusion coefficient has been calculated for the resolved waves (Grygalashvyly et al., 2012).
 79 Large effective diffusion has also been suggested based on scaling argument using high-
 80 resolution WACCM results (H.-L. Liu, 2017). The challenge for such modeling study is
 81 how to maintain the physical consistency between the resolved and parameterized GW
 82 effects (the gray zone challenge, (Vosper et al., 2016; H.-L. Liu, 2019)). A strategy to
 83 address this challenge is to deduce the effect by unresolved waves from the resolved wave
 84 effect based on scale invariance (H.-L. Liu, 2019). This method has been used to calcu-
 85 late the vertical flux of the GW horizontal momentum and the associated zonal forcing
 86 (H.-L. Liu, 2019). In this study, this method is applied to the calculation of vertical eddy
 87 diffusion by GWs.

88 2 Numerical Model

89 A high-resolution version of WACCM is used in this study. Detailed description
 90 of the model and simulations is found in H.-L. Liu et al. (2014) (and references therein).
 91 A brief summary is provided here. WACCM is one of the atmosphere components of the
 92 NCAR Community Earth System Model (CESM), with the vertical domain extending
 93 to 5.9×10^{-6} hPa (~ 145 km). The spectral element (SE) dynamical core is used in this
 94 study. It is based on a cubed-sphere, with a quasi-uniform horizontal resolution of ~ 25
 95 km and a 0.1 scale height vertical resolution above 40hPa (and higher below). A July
 96 simulation with parameterized wave drag (H.-L. Liu, 2017, 2019) is used for the current
 97 study. The gravity wave parameterization scheme used in the standard WACCM con-
 98 figuration (Richter et al., 2010) has been adjusted (H.-L. Liu, 2017) to obtain realistic
 99 mean wind and temperature structures.

100 3 Analysis

101 We first examine the zonal wavenumber power spectra of potential temperature θ
 102 and vertical wind w and their co-spectrum—the spectrum of vertical heat flux. From Fig-
 103 ure 1(a), it is seen that the power spectrum of θ ($P_\theta(k)$, k is the zonal wavenumber) fol-
 104 lows a power-law distribution between zonal wavenumber 10 and 100, with a slope of -
 105 1.9. This is similar to the power spectrum of potential temperature found in the tropo-
 106 sphere (Nastrom & Gage, 1985). The power spectrum of the vertical wind ($P_w(k)$) fol-
 107 lows a power-law with a much shallower slope (-0.7), as noted in previous studies (Bacmeister
 108 et al., 1996; Lane & Knievel, 2005; Lane & Moncrieff, 2008; H.-L. Liu, 2019). As in the
 109 case of the vertical momentum flux (H.-L. Liu, 2019), the shallow slope of the vertical

110 wind leads to a shallow spectrum of vertical heat flux. As seen in Figure 1(c): the ver-
 111 tical heat flux spectrum ($S_{w\theta}(k)$) has a slope of -1.3, which is the average value of the
 112 slopes of $P_\theta(k)$ and $P_w(k)$. Similar spectral features are found at other altitudes and lat-
 113 itudes, and Figures 1 (d-f) show the latitudinal dependence of spectral slopes of $P_\theta(k)$,
 114 $P_w(k)$, and $S_{w\theta}(k)$ at stratospheric, mesospheric and lower thermospheric altitudes (30,
 115 75, and 90 km, respectively), with the slope calculated using a method described in H.-
 116 L. Liu (2019). The latitudinal and height dependence of the spectral slope of $S_{w\theta}(k)$ are
 117 very similar to those of the vertical momentum flux (Figure 1 of H.-L. Liu (2019)): the
 118 spectral slope variability is larger at lower altitudes, and the largest deviation from the
 119 nominal “mean” value (downslope of 7/6) is found at southern (winter) stratosphere and
 120 lower mesosphere (below ~ 70 km), likely resulting from the “run-away” jet therein due
 121 to missing gravity wave forcing.

122 It is noted that the full spectrum of heat flux $S_{w\theta}(k)$ has both upward (positive)
 123 and downward (negative) values, corresponding to counter-gradient and down-gradient
 124 fluxes, respectively, with respect to zonal mean potential temperature ($\bar{\theta}$). Overall the
 125 down-gradient flux is larger than the counter-gradient flux, as expected, and the spec-
 126 tral components of the counter-gradient fluxes may result from flow transience, nonlin-
 127 earity, and its spectral transform. In Figure 1(c-f), only the down-gradient components
 128 and their slopes are plotted.

An effective vertical eddy diffusion coefficient, in the zonal mean sense, can be cal-
 culated from the heat flux and the vertical gradient of zonal mean potential tempera-
 ture

$$K_{zz} = -\overline{w'\theta'}/(\partial\bar{\theta}/\partial z) \quad (1)$$

with primes denoting perturbation around zonal mean. Here we will focus on the con-
 tribution from gravity waves, and the flux term can be calculated from spectral integra-
 tion between the cutoff zonal wavenumbers on the low and high ends, $k^<$ and $k^>$, re-
 spectively:

$$K_{zz}^{<>} = - \int_{k^<}^{k^>} S_{w\theta}(k) dk / (\partial\bar{\theta}/\partial z) \quad (1')$$

$k^<$ is set to 10 here, and $k^>$ should be set to 1000–2000 to cover the full mesoscale range.
 However, the model can only resolve wavenumber up to k^l due to limited model reso-
 lution. With a quasi-uniform resolution of ~ 25 km, the current model can effectively re-
 solve waves with horizontal wavelength of 200 to 250 km. The k^l is set to zonal wavenum-
 bers corresponding to wavelength 250 km at each latitude. Part of the total effective eddy
 diffusion coefficient $K_{zz}^{<>}$ can be directly calculated from the resolved waves, which is
 denoted as $K_{zz}^{<l}$, using Equation 1' but between wavenumber $k^<$ and k^l . On the other
 hand, the effective eddy diffusion coefficient from higher wavenumbers, $K_{zz}^{l>}$, cannot be
 properly accounted for because these waves are unresolved or under-resolved. However,
 it can be deduced from $K_{zz}^{<l}$ by using scale invariance, like the vertical flux of zonal mo-
 mentum and zonal forcing (H.-L. Liu, 2019):

$$K_{zz}^{l>}/K_{zz}^{<l} = \begin{cases} ((k^>/k^l)^{1-\alpha} - 1)/(1 - (k^</k^l)^{1-\alpha}) & \text{if } \alpha \neq 1 \\ \ln(k^>/k^l)/\ln(k^l/k^<) & \text{if } \alpha = 1 \end{cases} \quad (2)$$

129 where α is the down-slope value of the spectrum. As noted above, there are wave com-
 130 ponents with upward heat flux, and the apparent K_{zz} associated with these spectral com-
 131 ponents would be negative ($K_{zz}(k^-) < 0$). Both the positive and negative spectral val-
 132 ues, $K_{zz}(k^+)$ and $|K_{zz}(k^-)|$, display power-law distribution, though their slopes could
 133 be different. The spectral calculation described above is performed separately for the two,
 134 and then summed (with sign) to obtain the net K_{zz} .

135 Figures 2(a-c) show the K_{zz} by the resolved waves ($K_{zz}^{<l}$), by the under-/un-resolved
 136 waves deduced from Equation 2 ($K_{zz}^{l>}$), and the sum of the two. The parameterized K_{zz}

137 is shown in (d) for comparison. $K_{zz}^{<|}$ increases with altitude, from 10^{-3} – 10^{-2} m^2s^{-1} in
 138 the lower stratosphere to $\sim 10^2$ m^2s^{-1} in the lower thermosphere. Its latitude-height struc-
 139 ture is similar to that of the zonal forcing by gravity waves (H.-L. Liu, 2019). $K_{zz}^{>|}$ also
 140 has a similar spatial structure, and its magnitude is comparable to or even larger than
 141 $K_{zz}^{<|}$. $K_{zz}^{>|}$ is over 1000 m^2s^{-1} at high latitudes in the southern stratosphere and lower
 142 mesosphere. This is due to the over-flattening of the wave spectra therein, as can be seen
 143 from Figure 1(d). For example, the spectral slope is 0 around 50°S at 30 km, and ac-
 144 cording to Equation 2 $K_{zz}^{>|}$ would be ~ 10 times larger than $K_{zz}^{<|}$. This over-flattening
 145 of the wave spectra is caused by the unrealistically large winter jet, which is in turn due
 146 to insufficient gravity wave forcing (H.-L. Liu, 2019).

147 The total $K_{zz}^{<>}$ ($K_{zz}^{<|} + K_{zz}^{>|}$) has similar spatial structure and magnitude to the
 148 parameterized K_{zz}^P in the mesosphere (70–85 km) (though at SH higher latitudes the for-
 149 mer is generally larger). At altitudes below and above $K_{zz}^{<>}$ is larger than K_{zz}^P . This is
 150 because the parameterization used is based on the linear saturation theory for wave break-
 151 ing (Lindzen, 1981), and in WACCM it has been tuned so that much of the wave break-
 152 ing occurs around MLT to reverse the zonal wind. It is worth noting that the latitude/height
 153 structure of $K_{zz}^{<>}$ is in good agreement with that of the absolute momentum flux derived
 154 from satellite observations from the stratosphere to the lower thermosphere (Ern et al.,
 155 2018). $K_{zz}^{<>}$ is thus more realistic than K_{zz}^P .

Averages globally, over the northern/southern hemispheres (NH/SH) poleward of
 30° and over the tropical region of $K_{zz}^{<|}$, $K_{zz}^{>|}$, $K_{zz}^{<>}$, and K_{zz}^P are shown in Figure 3(a).
 The equivalent transport coefficient K_{adv} associated with the residual-mean vertical ve-
 locity, \overline{w}^r , is calculated as

$$K_{adv} = |\widehat{\overline{w}^r \overline{\theta}} / \frac{\partial \overline{\theta}}{\partial z}| \quad (3)$$

156 following Holton and Schoeberl (1988), and its area-weighted averages (hat sign) are shown
 157 in respective plots. It is noted that an alternative method is to define K_{adv} as $|\overline{w}^r \frac{\partial \overline{\theta}}{\partial z} / \frac{\partial^2 \overline{\theta}}{\partial z^2}|$,
 158 since this would apparently facilitate direct comparison of the advective term and the
 159 diffusive term. However, $\frac{\partial^2 \overline{\theta}}{\partial z^2}$ is close to 0 at some latitudes and altitudes, making it dif-
 160 ficult to interpret the result. On the other hand, at altitudes where this second order deriva-
 161 tive is finite, the transport coefficients calculated from the two methods are found to be
 162 comparable. The mean molecular diffusion is also plotted for comparison. By compar-
 163 ing the global mean of $K_{zz}^{<|}$ and $K_{zz}^{>|}$, it is seen that the two are comparable between ~ 70 –
 164 95 km, and the latter (diffusion by unresolved waves) is larger/smaller at lower/higher
 165 altitudes. As discussed earlier, $K_{zz}^{>|}$ becomes extremely large in the southern stratosphere
 166 and lower mesosphere at higher latitudes, where the wave spectra become excessively flat.
 167 This is also reflected in the global average. The total K_{zz} and K_{zz}^P are comparable at
 168 75 to 80 km. At lower altitudes, K_{zz}^P is 2–3 orders of magnitude less than the total K_{zz} ,
 169 and is actually similar to the molecular diffusion between 20 and 50 km. K_{zz}^P also de-
 170 creases rather quickly with altitude above 75 km, and crosses the molecular diffusion co-
 171 efficient profile at 90 km. The homopause height according to K_{zz}^P is thus 15–20 km too
 172 low compared with the accepted value (105–110 km) (Schunk & Nagy, 2009; Andrews
 173 et al., 1987). On the other hand, the total K_{zz} increases with altitude above 70 km, and
 174 becomes equal to the molecular diffusion coefficient profile at 103 km. In comparison with
 175 K_{adv} , the total K_{zz} is less at all altitudes below 100 km, except when it becomes unre-
 176 alistically large near ~ 50 km. This is consistent with the conclusion reached by Holton
 177 and Schoeberl (1988), that the vertical eddy diffusion is in general secondary to advec-
 178 tive transport. However, hemispheric and latitudinal dependence are noted in the com-
 179 parison (Figure 3(b-d)): K_{zz} and K_{adv} become more comparable in the winter hemisphere
 180 (SH) in the mesosphere and lower thermosphere (especially at higher latitudes). The NH
 181 and SH difference in K_{adv} results from the different temperature structure: The tem-
 182 perature increases with altitude at a faster rate—thus has a shorter vertical scale—in the
 183 winter MLT than in the summer, due to the adiabatic heating associated with the down-

184 welling driven by gravity wave drive. This result suggests that the vertical diffusion can
 185 play an important role in the vertical transport in winter time MLT at higher latitudes.

186 It is found that the total K_{zz} calculated using the method outlined here does not
 187 have a sensitive dependence on k^{\perp} . The K_{zz} shown in the figures is obtained by setting
 188 k^{\perp} to zonal wavenumbers corresponding to 250 km zonal wavelength for each latitude.
 189 The calculation has been repeated by changing the horizontal wavenumber to 400 km
 190 (with the small and large wavenumber cutoffs unchanged), and the total K_{zz} obtained
 191 is similar.

192 4 Discussion

193 The effective diffusion may result from gravity wave dissipation (Walterscheid, 1981)
 194 and dispersion by randomly superposed gravity waves (Walterscheid & Hocking, 1991;
 195 Lukovich & Shepherd, 2005). Nonlinearity can also lead to apparent transport, but it
 196 may not act coherently on the mean flow over time, and considerable cancelation may
 197 occur when averaged over time (Walterscheid & Hocking, 1991; Nakamura, 2001). As
 198 such, the diffusion coefficient deduced from wave flux calculation (Equation 1) (i) may
 199 vary significantly over time, and (ii) is not positive definite. This issue is examined here.
 200 As discussed in the previous section, down-gradient and counter-gradient fluxes are sep-
 201 arated when analyzing the heat flux spectrum, and so are the calculations of the diffu-
 202 sion coefficients by the resolved and unresolved waves. In Figure 4, the positive and neg-
 203 ative $K_{zz}^{<}$ and $K_{zz}^{>}$ and their sums are shown at several altitudes. The values in the NH
 204 and the SH are shown separately, since the $K_{zz}^{>}$ values in the two hemispheres can dif-
 205 fer significantly. It is seen from the figure that at all the altitudes and latitudes the to-
 206 tal $K_{zz}^{<}$ and $K_{zz}^{>}$ are positive, indicating the flux calculation using potential tempera-
 207 ture can indeed yield the net down-gradient flux. It is also seen that the values of the
 208 positive and negative K_{zz} (equivalently the down and counter gradient heat fluxes) are
 209 several times larger than the net values. This confirms the findings by Walterscheid and
 210 Hocking (1991) that there is considerable cancelation between the two.

211 Figure 4 also shows that the latitudinal dependence of $K_{zz}^{<}$ and $K_{zz}^{>}$ can be dif-
 212 ferent. For example, at 90 km $K_{zz}^{<}$ has similar values at the equator and at middle north-
 213 ern latitudes (net values between 10–20 m^2s^{-1}), but $K_{zz}^{>}$ values at middle northern lat-
 214 itudes is much larger than the equatorial values (over 30 m^2s^{-1} vs nearly 0). This is be-
 215 cause of the latitudinal dependence of the spectral slope. As seen from Figure 1(f), at
 216 90 km the slope is much flatter at middle northern latitudes (down slope value ~ 0.8) than
 217 at the equator (down slope value ~ 1.4). The spectral slopes of the positive and nega-
 218 tive K_{zz} (down and counter gradient fluxes) can also be different, with the former gen-
 219 erally flatter than the latter (thus the positive net $K_{zz}^{>}$ values).

220 The average eddy diffusion coefficient obtained here (Figure 3) is comparable to
 221 that deduced from observations in the MLT region. For example, the total K_{zz} shown
 222 in Figure 3(a) between 90–95 km is 30–50 m^2s^{-1} . Salinas et al. (2016) derived eddy dif-
 223 fusion from SABER CO_2 measurement, and it is $\sim 33 \text{ m}^2\text{s}^{-1}$ at 90 km. Swenson et al.
 224 (2019) obtained global mean eddy diffusion coefficient from O determined by SABER
 225 OH measurements, with odd oxygen loss considered, and the value is 33–60 m^2s^{-1} be-
 226 tween 90–95 km. This is smaller than the eddy diffusion coefficient from an earlier esti-
 227 mate without considering the odd oxygen loss (Swenson et al., 2018). It is also smaller
 228 than the mean eddy diffusion coefficient estimated from O determined from SCIAMACHY
 229 measurements (70–90 m^2s^{-1} for the same altitude range). It is worth noting that at 97
 230 km, the total K_{zz} from Figure 3(a) is $\sim 60 \text{ m}^2\text{s}^{-1}$. This is less than the eddy diffusion
 231 coefficient applied at the lower boundary of TIE-GCM (~ 97 km) by Qian et al. (2009),
 232 200–250 m^2s^{-1} around June solstice, to obtain agreement of the thermospheric density
 233 between TIE-GCM simulation and that inferred from satellite drag. However, the effec-
 234 tive diffusion coefficient obtained in that study is a measure of all dynamical effects not

235 included in the model, including large-scale processes such as mean circulation and tidal
 236 effects (Jones Jr. et al., 2017). For example, K_{adv} is between 100 and 200 m^2s^{-1} accord-
 237 ing to Figure 3(a).

238 As mentioned in the Introduction, previous numerical experiments suggested that
 239 the vertical eddy transport in WACCM tends to be too weak. For example, Feng et al.
 240 (2013) found from a 1-D model that an effective diffusion coefficient of $\sim 200 \text{ m}^2\text{s}^{-1}$ is
 241 needed for 80–90 km at mid-latitude to sustain a meteoric input of more than 20 td^{-1} ,
 242 while the parameterized K_{zz} from that WACCM version used was $5 \text{ m}^2\text{s}^{-1}$ and could
 243 only sustain a meteoric input of 2.1 td^{-1} . The total K_{zz} from the calculation presented
 244 in this study is $\sim 45/30 \text{ m}^2\text{s}^{-1}$ at 90km and 40°N/S . This is still less than the required
 245 value of $\sim 200 \text{ m}^2\text{s}^{-1}$. However, eddy diffusion is the only transport process considered
 246 in the 1-D model, and large-scale dynamics would account for a significant portion of the
 247 vertical transport. For example, the transport coefficient corresponding to the downward
 248 residual circulation in the winter hemisphere is between 45–80 m^2s^{-1} within the 80–90
 249 km altitude range (Figure 3(c)). Other studies also found the need to increase the pa-
 250 rameterized K_{zz} by decreasing the effective Prandtl number (Garcia et al., 2014; Orsolini
 251 et al., 2017; Smith-Johnsen et al., 2018). For example, a much better agreement between
 252 simulated and observed CO_2 in the MLT can be achieved when the Prandtl number is
 253 reduced by half, thus doubling the global mean K_{zz} from 7, 20, and 45 m^2s^{-1} to 14, 40
 254 and 90 m^2s^{-1} at 80, 90 and 100 km, respectively (Garcia et al., 2014). The latter set of
 255 values are comparable to the NH averaged values shown in Figure 3.

256 Vertical effective diffusivity (Nakamura, 2001) by gravity waves in the MLT has been
 257 computed from numerical experiments using an off-line coupled model of the dynamics
 258 and chemistry (Kuehlungsborn Mechanistic general Circulation Model–Mesospheric Chemistry-
 259 Transport Model, or KMCM-MECTM), both by full dynamical fields from the simula-
 260 tion and by dynamical fields with the resolved smaller scales (350–1000km) filtered out
 261 (Grygalashvily et al., 2012). The effective diffusion coefficients obtained, which are by
 262 waves with the horizontal scales between 350–1000 km, have spatial structures similar
 263 to the total K_{zz} in Figure 2, with an upward-poleward tilting mesosphere peak between
 264 60–90 km in the NH, a “mixing barrier” layer of ~ 5 km above, and further increases above
 265 that. The spatial structure in the winter hemisphere is also similar, except for the very
 266 large values found in the stratosphere and lower mesosphere “cold pole” in the current
 267 study. The MLT values from that study, however, are much larger than those obtained
 268 here, with mesospheric maximum values in the summer hemisphere over $350 \text{ m}^2\text{s}^{-1}$ at
 269 60° latitude between 80–85 km, and maximum in the winter hemisphere at 100 km reach-
 270 ing $500 \text{ m}^2\text{s}^{-1}$ at middle to high latitudes. They are also larger than the values deter-
 271 mined from observational and parameterization studies mentioned above. The larger val-
 272 ues would also imply a higher turbopause. The cause of this discrepancy is unclear and
 273 needs to be determined in future studies, when atmosphere constituents are included in
 274 high-resolution WACCM simulations.

275 5 Summary and Conclusion

276 The zonal wavenumber spectrum of the vertical heat flux calculated from a high-
 277 resolution WACCM simulation is shown to follow a power-law distribution in the resolved
 278 mesoscale range. The spectral slope varies with latitude and height, and is similar to the
 279 slope of the vertical flux of horizontal momentum flux (H.-L. Liu, 2019). They are shall-
 280 lower than the spectral slopes of zonal spectra of kinetic and potential energies, likely
 281 due to the flat vertical wind spectrum. The smaller scale waves can thus contribute sig-
 282 nificantly to the total vertical fluxes.

283 The vertical eddy diffusion coefficient (K_{zz}) is calculated from the ratio between
 284 the vertical heat flux and the vertical gradient of zonal mean potential temperature. The
 285 contribution from the resolved gravity waves to K_{zz} (and equivalently the vertical heat

286 flux), can be directly calculated from the co-spectra of potential temperature and ver-
287 tical wind. The contribution by under-resolved and unresolved waves can be deduced
288 from the resolved portion of the spectra based on scale invariance, following the method
289 discussed in H.-L. Liu (2019). The calculation is performed separately for the down-gradient
290 heat flux (positive K_{zz}) and for the counter-gradient flux (negative K_{zz}). The two have
291 large cancellations, and the net heat flux is down-gradient and the total K_{zz} is positive.
292 Eddy diffusion coefficients by smaller scale, unresolved waves are indeed comparable or
293 even larger than that by resolved waves.

294 The K_{zz} values are in general agreement with vertical eddy diffusion values deduced
295 from observational and parametric studies. The globally averaged total K_{zz} increases
296 consistently with altitude, and is equal to molecular diffusion at ~ 103 km, consistent with
297 the homopause altitude. This study thus provides a method to directly calculate the ef-
298 fective vertical diffusion by gravity waves when the waves are partially resolved by the
299 model. The total K_{zz} thus obtained are generally larger than that from gravity wave pa-
300 rameterization, except in the mesosphere where the two become comparable. This is prob-
301 ably because the gravity wave parameterization scheme in the model has been tuned to
302 reproduce the wind and temperature structures in the mesosphere/mesopause region.
303 The parameterized K_{zz} is thus likely underestimating the vertical transport in the lower
304 thermosphere, a region critical for controlling atmosphere-geospace mass exchange, as
305 well as the vertical transport below the mesosphere.

Figure 1. Zonal wavenumber power spectrum density (PSD) of (a) potential temperature and (b) vertical wind at the equator and 75 km altitude. (c): the zonal wavenumber spectrum of the vertical heat flux at the same location. The thin straight lines in the plots indicate the power-law slope, and the slope values are marked by the lines. Downslope values of the heat flux spectrum (solid line) and PSD of potential energy (dotted line) and vertical wind (dashed line) at (d) 30 km, (e) 75 km and (f) 90 km. These are averages over 7 days (3–9 July).

Figure 2. Effective diffusion coefficient by (a) resolved waves, (b) unresolved waves and (c) the sum of the two. (d): monthly mean parameterized eddy diffusion coefficient for July according to Garcia et al. (2007).

Figure 3. Averages (a) globally, over (b) NH and (d) SH poleward of 30° , and (c) the tropical region of the effective eddy diffusion coefficient by resolved waves (blue dotted line), unresolved waves (blue dashed line), and their sum (blue solid line). In comparison, the black solid line is the molecular diffusion, the red solid line is the parameterized eddy diffusion coefficient, and the black dash-dot line is the equivalent transport coefficient by residual-mean vertical velocity (Equation 3).

Figure 4. The down-gradient (dotted line) and counter-gradient (dashed line) eddy diffusion coefficients and their sum (solid line) by the resolved waves (red) and unresolved waves (navy blue) at (a, b) 30 km, (c, d) 75 km, and (e, f) 90 km, and for the NH (a, c, e) and the SH (b, d, f).

Acknowledgments

I thank Noboru Nakamura and Daniel Marsh for valuable discussions. This effort is partially supported by NASA Grants 80NSSC20K1323, 80NSSC20K0601, 80NSSC20K0633, 80NSSC17K0007, and NSF Grant OPP 1443726. National Center for Atmospheric Research is a major facility sponsored by the National Science Foundation under Cooperative Agreement No. 1852977. Numerical simulations were performed on NWSC/NCAR Yellowstone and Cheyenne Supercomputers with computing resources provided by the NCAR Strategic Capability (NSC) allocation and the Computational and Information Systems Laboratory (CISL) at NCAR. NCAR CESM/WACCM is an open-source community model, and is available at <https://doi.org/10.5065/D67H1H0V>. Model output used for this study is available at <https://doi.org/10.5065/rxae-ab06>.

References

- Alexander, M. J., Geller, M., McLandress, C., Polavarapu, S., Preusse, P., Sassi, F., . . . S.Watanabei (2010). Recent developments in gravity-wave effects in climate models and the global distribution of gravity-wave momentum flux from observations and models. *Quart. J. Roy. Meteor. Soc.*, *136*, 1103-1124.
- Andrews, D. G., Holton, J. R., & Leovy, C. B. (1987). *Middle atmosphere dynamics*. Orlando, Florida: Academic Press.
- Bacmeister, J. T., Eckermann, S. D., Newman, P. A., Lait, L., Chan, K. R., Loewenstein, M., . . . Gary, B. L. (1996). Stratospheric horizontal wavenumber spectra of winds, potential temperature, and atmospheric tracers observed by high-altitude aircraft. *Journal of Geophysical Research: Atmospheres*, *101*, 9441-9470. doi: 10.1029/95JD03835
- Baldwin, M. P., Gray, L. J., Dunkerton, T. J., Hamilton, K., Haynes, P. H., Randel, W. J., . . . Takahashi, M. (2001). The quasi-biennial oscillation. *Reviews of Geophysics*, *39*, 179-229. doi: 10.1029/1999RG000073
- Becker, E., & Vadas, S. E. (2018). Secondary gravity waves in the winter mesosphere: Results from a high-resolution global circulation model. *Journal of Geophysical Research: Atmospheres*, *123*, 2605-2627. doi: 10.1002/2017JD027460
- Dunkerton, T. J. (1982). Theory of the mesopause semiannual oscillation. *Journal of the Atmospheric Sciences*, *39*, 2681-2690.
- Ern, M., Trinh, Q. T., Preusse, P., Gille, J. C., Mlynczak, M. G., Russell III, J. M., & Riese, M. (2018). Gracile: a comprehensive climatology of atmospheric gravity wave parameters based on satellite limb soundings. *Earth System Science Data*, *10*, 857-892. doi: 10.5194/essd-10-857-2018
- Feng, W., Marsh, D. R., Chipperfield, M. P., Janches, D., Höffner, J., Yi, F., & Plane, J. M. C. (2013). A global atmospheric model of meteoric iron. *Journal of Geophysical Research: Atmospheres*, *118*, 9456-9474. doi: 10.1002/jgrd.50708
- García, R. R., López-Puertas, M., Funke, B., Marsh, D. R., Kinnison, D. E., Smith, A. K., & González-Galindo, F. (2014). On the distribution of CO₂ and CO in the mesosphere and lower thermosphere. *Journal of Geophysical Research: Atmospheres*, *119*, 5700-5718. doi: 10.1002/2013JD021208
- García, R. R., Marsh, D. R., Kinnison, D. E., Boville, B. A., & Sassi, F. (2007). Simulation of secular trends in the middle atmosphere, 1950-2003. *J. Geophys. Res.*, *112*. doi: 10.1029/2006JD007485
- Gardner, C. S., & Liu, A. Z. (2010). Wave-induced transport of atmospheric constituents and its effect on the mesospheric Na layer. *Journal of Geophysical Research: Atmospheres*, *115*. doi: 10.1029/2010JD014140
- Grygalashvyly, M., Becker, E., & Sonnemann, G. (2012). Gravity wave mixing and effective diffusivity for minor chemical constituents in the mesosphere/lower thermosphere. *Space Sci Rev*, *168*, 333-362. doi: 10.1007/s11214-011-9857-x

- 359 Holton, J. R. (1982). The role of gravity wave induced drag and diffusion in the mo-
 360 mentum budget of the mesosphere. *Journal of the Atmospheric Sciences*, *39*,
 361 791-799.
- 362 Holton, J. R. (1983). The influence of gravity wave breaking on the general circula-
 363 tion of the middle atmosphere. *Journal of the Atmospheric Sciences*, *40*, 2497-
 364 2507.
- 365 Holton, J. R., & Schoeberl, M. R. (1988). The role of gravity wave generated advec-
 366 tion and diffusion in transport of tracers in the mesosphere. *Journal of Geo-
 367 physical Research*, *93*, 11075–11082.
- 368 Jones Jr., M., Emmert, J. T., Drob, D. P., & Siskind, D. E. (2017). Middle
 369 atmosphere dynamical sources of the semiannual oscillation in the ther-
 370 mosphere and ionosphere. *Geophysical Research Letters*, *44*, 12-21. doi:
 371 10.1002/2016GL071741
- 372 Lane, T. P., & Knievel, J. C. (2005). Some effects of model resolution on simulated
 373 gravity waves generated by deep, mesoscale convection. *Journal of the Atmo-
 374 spheric Sciences*, *62*, 3408-3419. doi: 10.1175/JAS3513.1
- 375 Lane, T. P., & Moncrieff, M. W. (2008). Stratospheric Gravity Waves Generated
 376 by Multiscale Tropical Convection. *Journal of the Atmospheric Sciences*, *65*,
 377 2598-2614. doi: 10.1175/2007JAS2601.1
- 378 Lindzen, R. S. (1981). Turbulence and stress owing to gravity wave and tidal break-
 379 down. *J. Geophys. Res.*, *86*, 9707-9714.
- 380 Liu, A. Z. (2009). Estimate eddy diffusion coefficients from gravity wave vertical
 381 momentum and heat fluxes. *Geophysical Research Letters*, *36*. doi: 10.1029/
 382 2009GL037495
- 383 Liu, H.-L. (2017). Large wind shears and their implications for diffusion in regions
 384 with enhanced static stability: The mesopause and the tropopause. *Journal of
 385 Geophysical Research: Atmospheres*, *122*, 9579–9590. (2017JD026748) doi: 10
 386 .1002/2017JD026748
- 387 Liu, H.-L. (2019). Quantifying gravity wave forcing using scale invariance. *Nature
 388 Communications*, *10*, 2605. doi: 10.1038/s41467-019-10527-z
- 389 Liu, H.-L., McInerney, J. M., Santos, S., Lauritzen, P. H., Taylor, M. A., & Pe-
 390 datella, N. M. (2014). Gravity waves simulated by high-resolution Whole
 391 Atmosphere Community Climate Model. *Geophysical Research Letters*, *41*,
 392 9106–9112. (2014GL062468) doi: 10.1002/2014GL062468
- 393 Lukovich, J. V., & Shepherd, T. G. (2005). Stirring and mixing in two-dimensional
 394 divergent flow. *Journal of the Atmospheric Sciences*, *62*, 3933-3954. doi: 10
 395 .1175/JAS3580.1
- 396 Nakamura, N. (2001). A New Look at Eddy Diffusivity as a Mixing Diagnos-
 397 tic. *Journal of the Atmospheric Sciences*, *58*, 3685-3701. doi: 10.1175/
 398 1520-0469(2001)058(3685:ANLAED)2.0.CO;2
- 399 Nastrom, G. D., & Gage, K. S. (1985). A climatology of atmospheric wavenumber
 400 spectra of wind and temperature observed by commercial aircraft. *Journal of
 401 the Atmospheric Sciences*, *42*, 950-960. doi: 10.1175/1520-0469(1985)042(0950:
 402 ACOAWS)2.0.CO;2
- 403 Orsolini, Y. J., Limpasuvan, V., Pérot, K., Espy, P., Hibbins, R., Lossow, S., ...
 404 Murtagh, D. (2017). Modelling the descent of nitric oxide during the el-
 405 evated stratopause event of January 2013. *Journal of Atmospheric and
 406 Solar-Terrestrial Physics*, *155*, 50-61. doi: [http://dx.doi.org/10.1016/
 407 j.jastp.2017.01.006](http://dx.doi.org/10.1016/j.jastp.2017.01.006)
- 408 Qian, L. Y., Solomon, S. C., & Kane, T. J. (2009). Seasonal variation of thermo-
 409 spheric density and composition. *Journal of Geophysical Research*, *114*. doi:
 410 10.1029/2008JA013643
- 411 Randall, C. E., Harvey, V. L., Holt, L. A., Marsh, D. R., Kinnison, D., Funke, B.,
 412 & Bernath, P. F. (2015). Simulation of energetic particle precipitation effects
 413 during the 2003?2004 arctic winter. *Journal of Geophysical Research: Space*

- 414 *Physics*, 120, 5035-5048. doi: 10.1002/2015JA021196
- 415 Richter, J. H., Sassi, F., & Garcia, R. R. (2010). Toward a physically based gravity
416 wave source parameterization in a general circulation model. *Journal of the At-*
417 *mospheric Sciences*, 67, 136-156. doi: 10.1175/2009JAS3112.1
- 418 Salinas, C. C. J. H., Chang, L. C., Liang, M.-C., Yue, J., Russell III, J., &
419 Mlynczak, M. (2016). Impacts of saber co2-based eddy diffusion coefficients in
420 the lower thermosphere on the ionosphere/thermosphere. *Journal of Geophys-*
421 *ical Research: Space Physics*, 121, 12,080-12,092. doi: 10.1002/2016JA023161
- 422 Sassi, F., & Garcia, R. R. (1997). The Role of Equatorial Waves Forced by Convec-
423 tion in the Tropical Semiannual Oscillation. *Journal of the Atmospheric Sci-*
424 *ences*, 54(15), 1925-1942. doi: 10.1175/1520-0469(1997)054<1925:TROEWF>2
425 .0.CO;2
- 426 Schunk, R. W., & Nagy, A. F. (2009). *Ionospheres, physics, plasma physics, and*
427 *chemistry (2nd ed.)*. Cambridge, UK: Cambridge University Press.
- 428 Smith-Johnsen, C., Marsh, D. R., Orsolini, Y., Tyssøy, H. N., Hendrickx, K., San-
429 danger, M. I., ... Stordal, F. (2018). Nitric oxide response to the april 2010
430 electron precipitation event: Using waccm and waccm-d with and without
431 medium-energy electrons. *Journal of Geophysical Research: Space Physics*,
432 123, 5232-5245. doi: 10.1029/2018JA025418
- 433 Swenson, G. R., Salinas, C. C. J. H., Vargas, F., Zhu, Y., Kaufmann, M., Jones Jr.,
434 M., ... Yee, J. H. (2019). Determination of global mean eddy diffusive trans-
435 port in the mesosphere and lower thermosphere from atomic oxygen and car-
436 bon dioxide climatologies. *Journal of Geophysical Research: Atmospheres*,
437 124(23). doi: 10.1029/2019JD031329
- 438 Swenson, G. R., Yee, Y., Vargas, F., & Liu, A. (2018). Vertical diffusion transport
439 of atomic oxygen in the mesopause region consistent with chemical losses and
440 continuity: Global mean and inter-annual variability. *Journal of Atmospheric*
441 *and Solar-Terrestrial Physics*, 178, 47-57.
- 442 Vosper, S. B., Brown, A. R., & Webster, S. (2016). Orographic drag on islands
443 in the nwp mountain grey zone. *Quarterly Journal of the Royal Meteorological*
444 *Society*, 142, 3128-3137. doi: 10.1002/qj.2894
- 445 Walterscheid, R. L. (1981). Dynamical cooling induced by dissipating internal
446 gravity-waves. *Geophysical Research Letters*, 8, 1235-1238.
- 447 Walterscheid, R. L., & Hocking, W. K. (1991). Stokes diffusion by atmospheric in-
448 ternal gravity waves. *Journal of the Atmospheric Sciences*, 48, 2213-2230.

Figure 1.

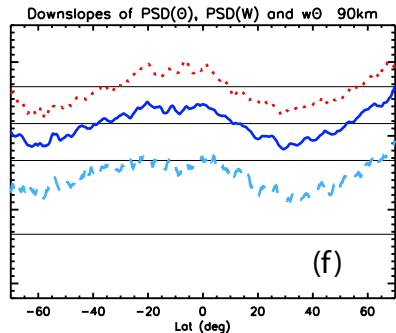
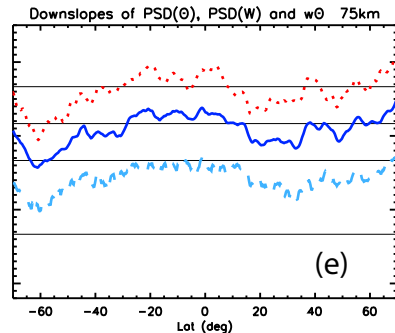
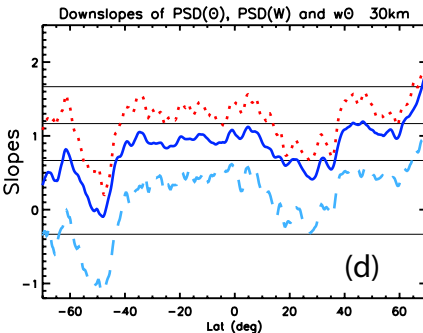
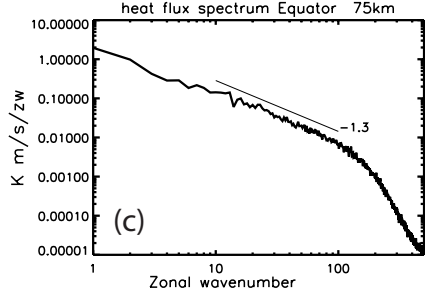
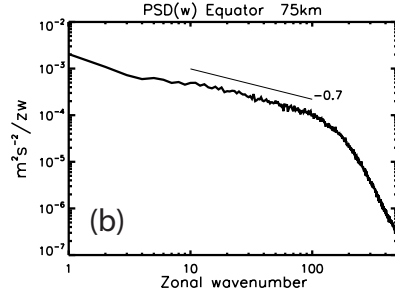
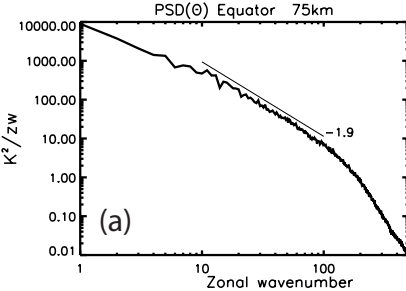


Figure 2.

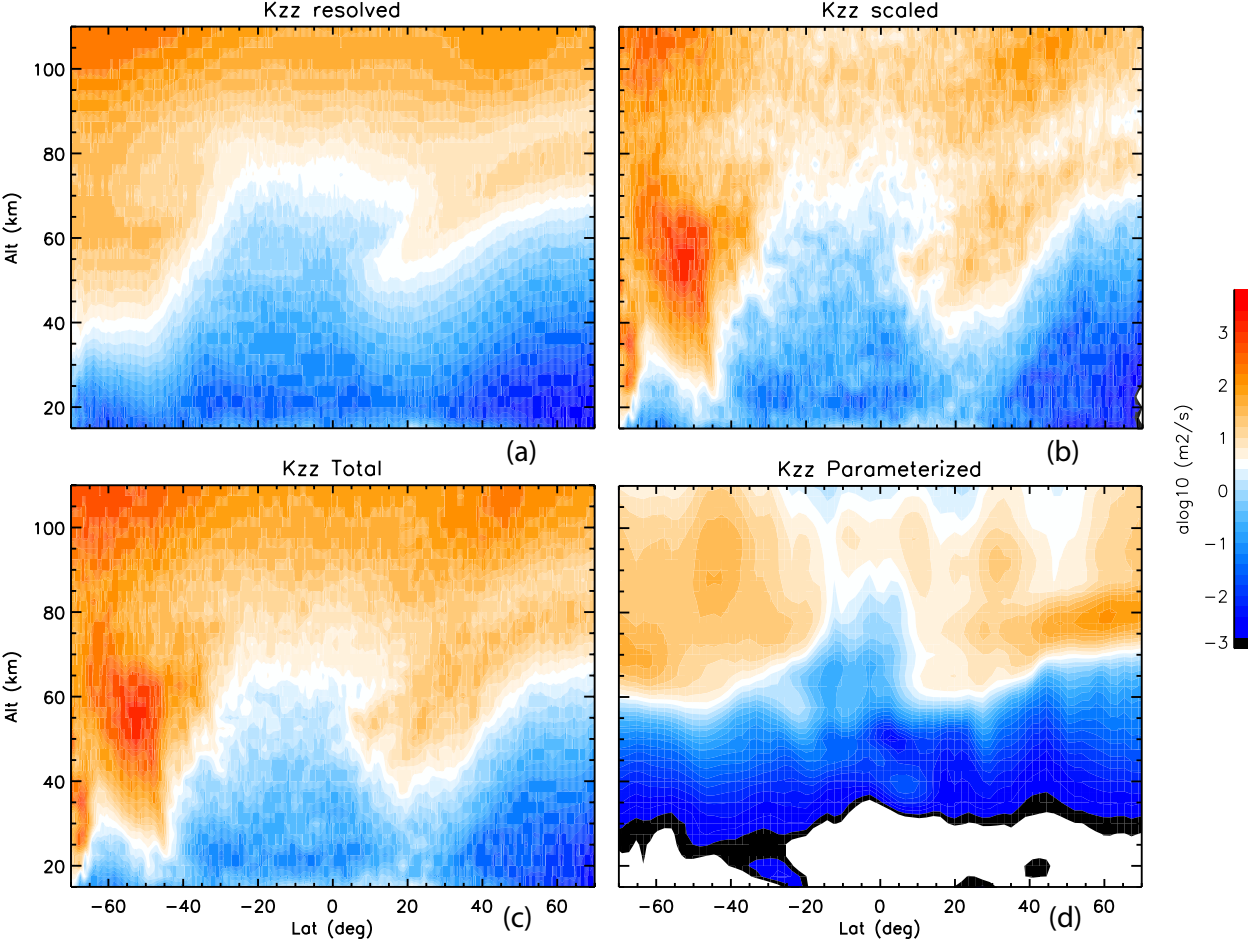
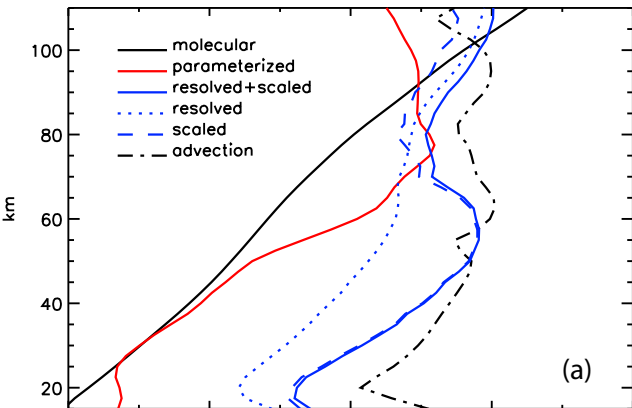
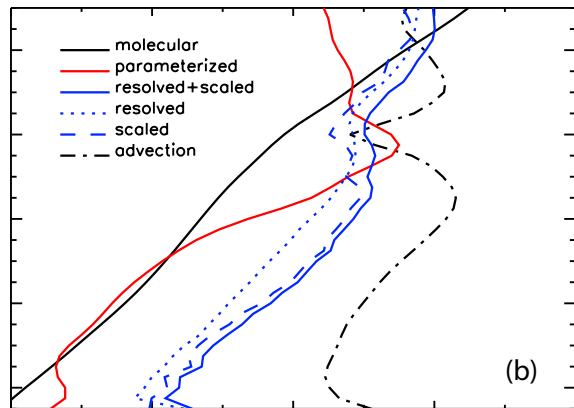


Figure 3.

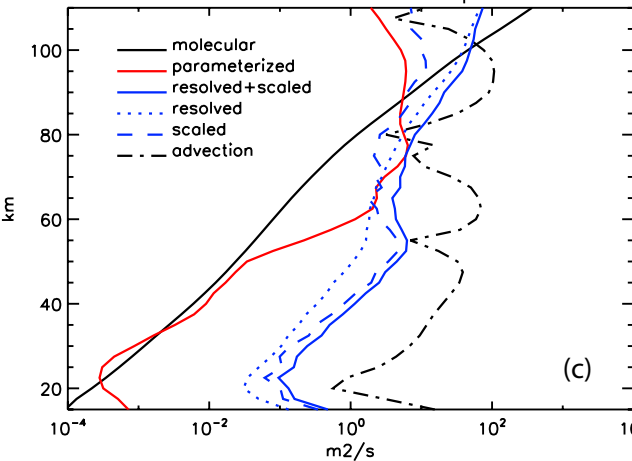
Diffusion coefficients Global



Diffusion coefficients NH



Diffusion coefficients Tropical



Diffusion coefficients SH

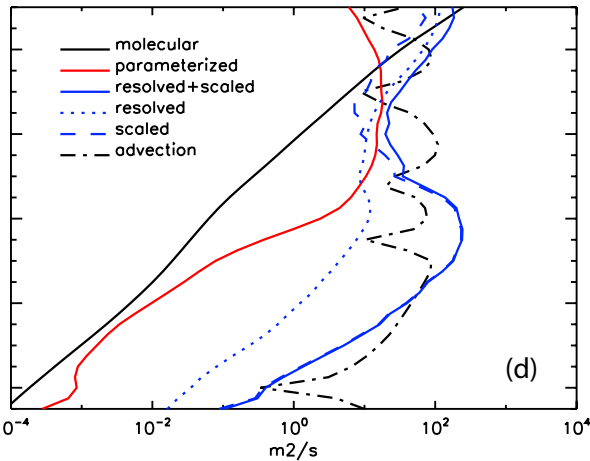


Figure 4.

